applied sciences

MDPI

Article

Study on Non-Stationary Wind Speed Models and Wind Load Design Parameters Based on Data from the Beijing 325 m Meteorological Tower, 1991–2020

Shihan Yang [1], Xiaodong Ji [1,2,*], Yifan Tao [3], Jingjing Jia [3], Zeyu Zhang [1] and Li Jiang [1]

[1] School of Soil and Water Conservation, Beijing Forestry University, Beijing 100083, China; y199992@bjfu.edu.cn (S.Y.); zhangzeyu1997@bjfu.edu.cn (Z.Z.); jiangli@bjfu.edu.cn (L.J.)
[2] Key Laboratory of State Forestry Administration on Soil and Water Conservation, Beijing Forestry University, Beijing 100083, China
[3] Institute of Atmospheric Physics, Chinese Academy of Sciences, Beijing 100029, China; taoyifan@mail.iap.ac.cn (Y.T.); jiajingjing@mail.iap.ac.cn (J.J.)
* Correspondence: jixiaodong@bjfu.edu.cn

Abstract: As the capital of China and a densely populated major city, the characteristics of Beijing's near-surface wind field change significantly with the increase in the density of underlying urban structures. The high randomness of natural wind makes it extremely difficult to develop a universally applicable wind-resistant load design code based on topographic factors and architectural features. This article takes the wind speeds recorded at 15 different height levels within the urban area by the 325 m meteorological tower in Beijing from 1991 to 2020 as the research subject. It quantifies the wind speed trends at different heights and introduces time-varying functions to establish a non-stationary wind speed model based on the optimal model. Additionally, it compares the basic wind speeds and wind pressure height variation coefficients obtained from measurements with the standards. The results show that, during the past 30 years of urbanization, the near-surface wind speed in the Beijing area has shown a decreasing trend. The model incorporating time-varying functions exhibited the best fit and demonstrated good predictive capabilities, with its calculated basic wind speeds being relatively high. The wind pressure height variation coefficient values in Beijing are between Class C and Class D terrains, being closer to Class C at lower altitudes. The conclusion reveals that urbanization has a significant impact on wind speeds, primarily concentrated at lower height levels, and that the basic wind speeds calculated based on standards underestimate the actual conditions when this impact is not considered. Although the average wind speed's wind profile index across the entire time series is mostly greater than the fixed value of 0.3 given by Class D, this represents an overestimated wind profile index for maximum wind speeds.

Keywords: wind speed; non-stationary model; time-varying function; wind pressure height variation coefficient; standard value; Beijing 325 m meteorological tower

check for updates

Citation: Yang, S.; Ji, X.; Tao, Y.; Jia, J.; Zhang, Z.; Jiang, L. Study on Non-Stationary Wind Speed Models and Wind Load Design Parameters Based on Data from the Beijing 325 m Meteorological Tower, 1991–2020. *Appl. Sci.* **2024**, *14*, 3979. https://doi.org/10.3390/app14103979

Academic Editor: Maciej Dutkiewicz

Received: 18 March 2024
Revised: 3 May 2024
Accepted: 6 May 2024
Published: 8 May 2024

Copyright: © 2024 by the authors. Licensee MDPI, Basel, Switzerland. This article is an open access article distributed under the terms and conditions of the Creative Commons Attribution (CC BY) license (https://creativecommons.org/licenses/by/4.0/).

1. Introduction

The accelerated process of urbanization is faced with the problems of limited land resources and business needs in economic development, thus contributing to a large extent to the growth of demand for high-rise buildings, which is a response to the needs of the urban economy, as well as social development [1,2]. As global climate change intensifies, the design and construction of high-rise buildings increasingly need to take into account the impacts of extreme weather events, especially changes in wind speed, which directly influence the structural safety and comfort of high-rise buildings [3,4].

As the capital city of China and a densely populated city, the near-surface wind field characteristics of Beijing change significantly with the increasing density of urban structures [5]. In addition, due to the strong randomness of natural winds, it is very difficult

to develop a universally applicable wind load design code based only on topographic coefficients and building characteristics for the wind-resistant design of buildings [6,7]. Wind field characteristics are the basis for the study of wind loads and provide the basic information that influences the magnitude and distribution of wind loads [8,9]. In this context, long-term, actual wind speed observations across multiple altitude levels and studies of measured wind field characteristics are essential.

Wind load is the actual wind force acting on a building or structure, which is determined by a combination of varying wind speeds and directions, as well as the shape, size, and surface roughness of the building [10–12]. In the calculation of wind loads, on the one hand, the dynamic response of the structure, including the vibrations and deformations caused by wind, as well as the architectural features, is primarily addressed through a modal analysis and computational fluid dynamics (CFD) [13–15]. On the other hand, the calculation of wind loads is based on the determination of basic wind pressure, which is a theoretical value derived from wind field characteristics according to Bernoulli's equation and can be calculated from basic wind speed, air density, and dimensionless coefficients [16,17]. In architecture and engineering design, basic wind speed, defined as the speed not to be exceeded during a specific return period (usually 50 or 100 years), is used as a reference value for the calculation of wind loads [18,19]. Extreme value models allow us to estimate the maximum wind speed over these long return periods, thereby determining the basic wind speed [20,21]. However, due to the stochastic nature of wind speeds and limited wind speed samples, it is difficult to determine the most universally suitable probability distribution model, and many studies have been conducted to compare different distribution models and evaluate the most suitable one through parametric tests [22–24]. In order to improve the performance of the models, many scholars have paid attention to joint probability distributions, such as the joint probability distributions of wind speeds at two different locations in space or time, or the study of wind speeds in combination with covariates such as wind direction and the wind shear index [25,26]. In the study of extreme value models, the traditional smooth model assumes that the data are smooth in time and that their statistical properties do not vary over time [27]. However, under the effect of factors such as climate change and urbanization, the characteristics of extreme wind speeds may change due to long-term trends, cyclical changes in wind speeds, etc., at which time the distribution model of wind speeds may also change [28,29]. Non-stationary extreme value models allow for the probability distribution of extremes, such as maxima or minima, to vary over time, environmental conditions, or other influencing factors. These models typically require more complex mathematical and statistical methods for estimation and validation, including a time-series analysis and nonlinear regression models [30–32]. In the context of wind speed studies, non-stationary extreme value models leverage historical data to identify and model the trends of extreme wind speed distributions over time, enabling the analysis and prediction of how the frequency and intensity of extreme wind speed events change over time [33–35].

Current research on wind speed models based on actual measurements has made some progress. Huang et al. estimated a joint probability distribution model of monsoon fluctuating wind speeds using data recorded by an anemometer installed at the top of the SWFC building in Shanghai, China, at a height of 497 m, representing the wind speed frequency components as a mixture distribution model consisting of the Gaussian distribution and generalized Pareto distribution [36]. Natarajan et al. studied wind speeds measured at ten different elevations in Tamil Nadu, India, and noted that a single distribution could not fit all sites, whereas the generalized extreme value distribution performed well at most sites [37]. Wang et al. collected wind speed samples from 10 m to 19 m heights over three years using a lidar wind measurement system in the suburbs of Hohhot, China, and derived a new wind power density estimation formula based on a three-parameter Weibull distribution [38].

However, current research on the application of extreme value theory in long-term changing complex urban environments is insufficient, with most models being stationary

models established from short-term measured data. Additionally, existing empirical studies on wind speeds mostly focus on specific heights, with relatively limited research on the long-term variability of wind speeds across different atmospheric levels. At this time, the calculation of design wind loads at different heights can only be completed using empirical wind pressure height variation coefficients based on terrain classification.

Based on this, this paper uses long-term wind speed data collected from 15 different height levels on the 325 m meteorological tower in Beijing from 1991 to 2020 to quantify the trends in wind field characteristics in the Beijing urban area over nearly 30 years. It compares the goodness of fit of standards and traditional wind speed models, incorporating time-varying functions into the optimal wind speed model to account for wind speed trends. The study explores the impacts of urbanization and climate change on wind speeds, combining wind speed measurement data at different height levels with the optimal wind speed model to obtain wind pressure height variation coefficients and compare them with standards. This aims to assess the applicability of standards to architectural design in central Beijing and provide theoretical and data support for wind-resistant design in high-rise buildings in the context of rapid development.

2. Materials and Methods

2.1. Study Area

Built in August 1979, the 325 m Beijing meteorological tower is in the center of Beijing (39°58′ N, 116°22′ E), with an altitude of 49 m above sea level, about 1 km from the North Third Ring Road. The tower is equipped with 15 observation platforms at different heights: 8 m, 15 m, 32 m, 47 m, 65 m, 80 m, 100 m, 120 m, 140 m, 160 m, 180 m, 200 m, 240 m, 280 m, and 320 m. Until the 1990s, the area was a suburb, with a lack of tall buildings in the vicinity, and buildings over 20 m were located more than 1 km away. However, with the rapid urbanization of Beijing, the meteorological tower has witnessed a significant change in the surrounding environment, from a relatively simple subsurface in the past to a complex and rough subsurface today. This change not only marks the rapid development of Beijing's urbanization but also reflects the transformation of the area where the meteorological tower is located from a suburban to a dense urban environment. Figure 1 shows the geographical location of the 325 m meteorological tower and a comparison of the changes in its surrounding environment from the 1970s to the present.

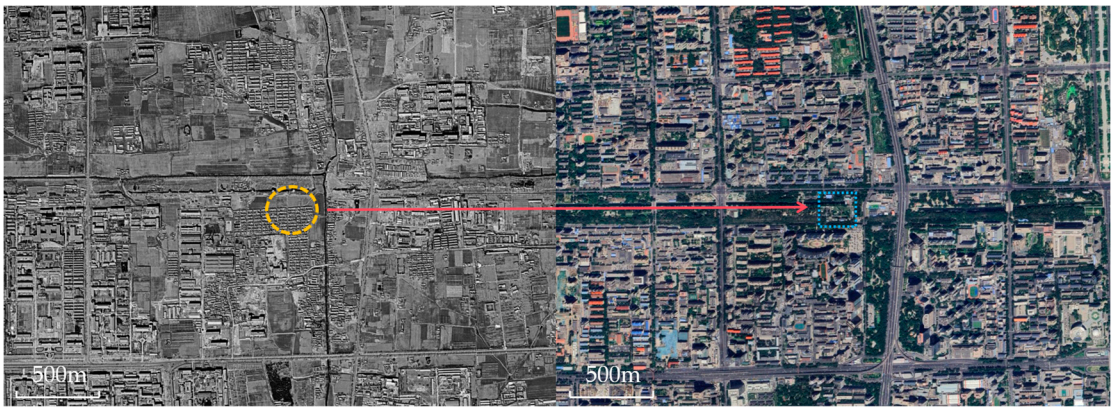


Figure 1. Comparative satellite imagery of the 325 m meteorological tower area in March 1973 (USGS Landsat, yellow box marking the proposed site of the meteorological tower) and June 2023 (accessed from https://earth.google.com/ on 20 February 2024, blue box marking the location of the meteorological tower).

2.2. Data

This article uses wind speed data collected from 15 different height levels ranging from 8 m to 320 m at the Beijing 325 m meteorological tower. Each platform of the tower is equipped with anemometers in a dual arm configuration in the two prevailing wind

directions (southeast and northwest), with simultaneous data collection at each height and a sampling frequency of 20 s. This design effectively reduces the interference of the tower structure on the wind speed measurements. The wind speed data are averaged every ten minutes, aggregated into an hourly set, and there are 24 sets of data at each height level every day. To systematically analyze the trend of wind speed changes in the urban area of Beijing over the past thirty years, data from specific years were selected, namely 1991, 1995, 2000, 2005, 2010, 2015, and 2020 (1990 was replaced by 1991 due to significant data loss caused by equipment maintenance). Figure 2 shows the Beijing 325 m meteorological tower.



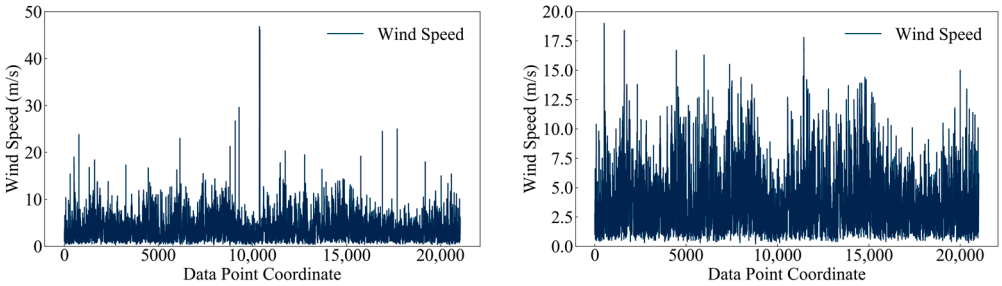
Figure 2. The Beijing 325 m meteorological tower.

High-frequency sampling captures environmental noise, such as equipment vibration and nearby traffic flow, which can distort the true values in the data. Additionally, the long-term use of instruments and certain sudden extreme weather events can also cause data anomalies. For the accuracy of the analysis, the first step was quality control of the data, with the following process:

1. Stagnation value removal: In the time series data, if the measurement value remains unchanged over a period, it often indicates a failure in the sensor, signal transmission, or instrument operation. This continuous unchanging measurement value is defined as a stagnation value. Identify data points in the series where the difference from the stagnation value is greater than 0.5 and remove the data segment from the stagnation value starting point to the point before it.
2. Outlier removal: Based on the historical climatic statistical characteristics of the Beijing area, wind speed values greater than 50 m/s are defined as outliers and are directly removed.
3. Temporal continuity control: For a series of consecutive data points, calculate the difference between a point and the weighted average of its four contiguous points. If this difference exceeds the set threshold (5 m/s for wind speed), the point is considered discontinuous, and a central four-point interpolation is used to replace the value of that point with the calculated weighted average.
4. Spatial continuity control: When the location of an outlier does not allow for central four-point interpolation, and if data at other heights at the current location are complete, use the spatial continuity and surrounding height layer valid measurement data to estimate and fill missing data points through spline interpolation.

Figure 3 shows a comparison of the effects before and after the correction of the measured wind speed data (taking the wind speed data at 100 m height from 1991 to 2000 as an example). After quality control, the wind speed dataset is now representative enough

to support reliable statistical analysis (with a usable data ratio greater than 95%). The total remaining missing values and the total data count after processing are shown in Table 1.



(**a**) (**b**)

Figure 3. Comparative analysis of wind speeds at 100 m: 1991–2000 before and after processing. (**a**) Raw wind speed data. (**b**) Wind speed data after outlier removal.

Table 1. Remaining missing values and total data counts after processing.

Y_n	T_n	M_n	p (%)
1991	88,575	3066	96.5
1995	109,215	3348	96.9
2000	123,000	3003	97.6
2005	122,040	3442	97.2
2010	123,075	2366	98.1
2015	129,885	2092	98.4
2020	129,855	3294	97.5

Y_n—number of years; T_n—total number of data; M_n—total number of missing values; p—percentage of missing values.

2.3. Methodology

2.3.1. Wind Profile

The distribution of wind speed with height is known as the wind profile. In typical cases, friction on the ground reduces the wind speed in the lower atmosphere. In order to study the variation in the wind field in time series, power law wind profile theory is used to assess the variation in the wind speed at different heights [39], as shown in Equation (1):

$$\frac{v(z)}{v\left(z_{ref}\right)} = \left(\frac{z}{z_{ref}}\right)^{\alpha} \tag{1}$$

where $v(z)$ is the wind speed at height z; $v(z_{ref})$ is the wind speed at the reference height z_{ref}; and α is the wind shear index, which depends on the surface roughness and atmospheric stability.

2.3.2. Maximum Value Sampling

Due to the randomness of wind in nature and its physical generation process's autocorrelation over long time scales, assume a set of continuous random variables $Y_1, Y_2, \ldots, Y_n$ representing wind speeds at different time points. Their distribution may change over time due to seasonal variations. In this context, maximum value sampling is introduced to handle the complexity.

Under the maximum value sampling framework, the data are divided into consecutive blocks (each block representing a month or a day), each containing all wind speed values Y_i within that period. Define $V_{\max}$ as the maximum wind speed in each block:

$$V_{max} = max(Y_1, Y_2, \ldots, Y_n) \tag{2}$$

At this time, the distribution of V_{max} will be influenced by the distribution characteristics of Y_i. This method allows us to capture the strongest wind speeds that might be encountered in each period, while considering the autocorrelation and distribution changes of wind speed data within these periods. Although the original Y_i variables may follow different distributions and exhibit time dependence, we do not directly assume that the original wind speed data are independently and identically distributed. Instead, using the block sampling method, we focus on the extreme values V_{max} within each period, which then allows us to apply extreme value theory for subsequent analysis.

2.3.3. Trend Analysis

A trend analysis can describe the temporal variation in wind speed, and we use the least squares method and the Mann–Kendall trend test as a trend analysis method [40–42]. In the least squares method, we want to find a linear relationship, $y = kx + b$, such that the line is as close as possible to all data points. Parameters k and b of the linear relationship can be estimated by minimizing the sum of the squares of the differences between the actual observations y_i and the predictions of the linear model. This can be expressed as solving the following system of equations to obtain least squares estimate:

$$\begin{cases} k = \frac{\sum_{i=1}^{n} x_i y_i - \frac{\sum_{i=1}^{n} x_i \sum_{i=1}^{n} y_i}{n}}{\sum_{i=1}^{n} x_i^2 - \frac{\left(\sum_{i=1}^{n} x_i\right)^2}{n}} \\ b = \frac{\sum_{i=1}^{n} y_i}{n} - k\frac{\sum_{i=1}^{n} x_i}{n} \end{cases} \tag{3}$$

where k is the slope, and b is the intercept. If k is greater than 0, the random variables tend to be positively correlated; if k is less than 0, the random variables tend to be negatively correlated.

In the Mann–Kendall Trend Test, for given wind speed time series data, $v_1, v_2, \ldots, v_n$, the statistic S is defined as

$$S = \sum_{i=1}^{n-1} \sum_{j=i+1}^{n} sgn(v_j - v_i) \tag{4}$$

for each difference value, we compute the sign function according to Equation (5):

$$sgn(v_j - v_i) = \begin{cases} 1, if\ v_j > v_i \\ 0,\ if\ v_j = v_i \\ -1,\ if\ v_j < v_i \end{cases} \tag{5}$$

The trend analysis Z statistic was calculated using Equation (6), where $Var(S)$ is the variance in statistic s, calculated using Equation (7):

$$Z = \begin{cases} \frac{S-1}{\sqrt{Var(S)}}, if\ S > 0 \\ \frac{S+1}{\sqrt{Var(S)}},\ if\ S < 0 \\ 0,\ if\ S = 0 \end{cases} \tag{6}$$

$$Var(S) = \frac{n(n-1)(2n+5) - \sum_{p=1}^{q} t_p(t_p - 1)(2t_p + 5)}{18} \tag{7}$$

where n is the length of the sequence, q is the number of equal data groups in the sequence, and t_p is the number of data points in group p of equal data. Subsequently, the significance of the trend is determined based on the Z value and the chosen significance level.

2.3.4. Extreme Value Model

The generalized extreme value (GEV) distribution is a continuous probability distribution used for simulating and analyzing extreme value data [43]. The GEV distribution integrates three types of extreme value distributions, namely Gumbel, Fréchet, and the

inverted Weibull, which is also known as Type III extreme value distribution (used for minima but often transformed to represent maxima), providing a more general framework for extreme value modeling. The cumulative distribution function (CDF) of the GEV distribution is calculated using Equation (8):

$$F(x;\mu,\sigma,\xi) = exp\left(-\left[1+\xi\left(\frac{x-\mu}{\sigma}\right)\right]^{-1/\xi}\right), \text{ for } 1+\xi(x-\mu)/\sigma > 0 \quad (8)$$

where x is the random variable, μ is the location parameter, σ is the scale parameter, and ξ is the shape parameter. When ξ equals 0, the GEV distribution simplifies to the Gumbel distribution. When ξ is greater than 0, the GEV distribution becomes the Fréchet distribution. When ξ is less than 0, the GEV distribution corresponds to the inverted Weibull distribution.

2.3.5. Effectiveness Assessment

The negative log-likelihood (NLL) value is an important metric for evaluating statistical models, based on the probability (likelihood) of the model generating observed data to measure the goodness of fit of the data in model fitting [44]. The calculation of the NLL value is based on the maximum likelihood estimation (MLE), where the likelihood function is defined as the probability of observing data X given parameter θ, as shown in Equation (9):

$$L(\theta;X) = \prod_{i=1}^{n} f(x_I;\theta) \quad (9)$$

where θ represents the model parameter. Since the product operation may lead to numerical underflow, we typically take the logarithm of the likelihood function to convert it into a sum form, i.e., the log-likelihood function. In maximum likelihood estimation (MLE), our goal is to find the parameters that maximize the likelihood function. Similarly, we can achieve this by minimizing the negative log-likelihood (NLL) function, as shown in Equation (10):

$$\begin{cases} logL(\theta;X) = \sum_{i=1}^{n} logf(x_I;\theta) \\ NLL(\theta;X) = -\sum_{i=1}^{n} logf(x_I;\theta) \end{cases} \quad (10)$$

In different models, a lower NLL value indicates that the model's parameter settings are more likely to generate the observed data. However, when we adopt more complex models (such as non-stationary extreme value models), due to having more parameters, there might be a phenomenon of overfitting, which also leads to a lower NLL value, but this does not mean that the model performs better. Therefore, we introduce evaluation criteria that penalize complexity, namely, the Akaike information criterion (AIC) and the Bayesian information criterion (BIC), as shown in Equations (11) and (12):

$$AIC = 2k - 2ln(L) \quad (11)$$

$$BIC = ln(n)k - 2ln(L) \quad (12)$$

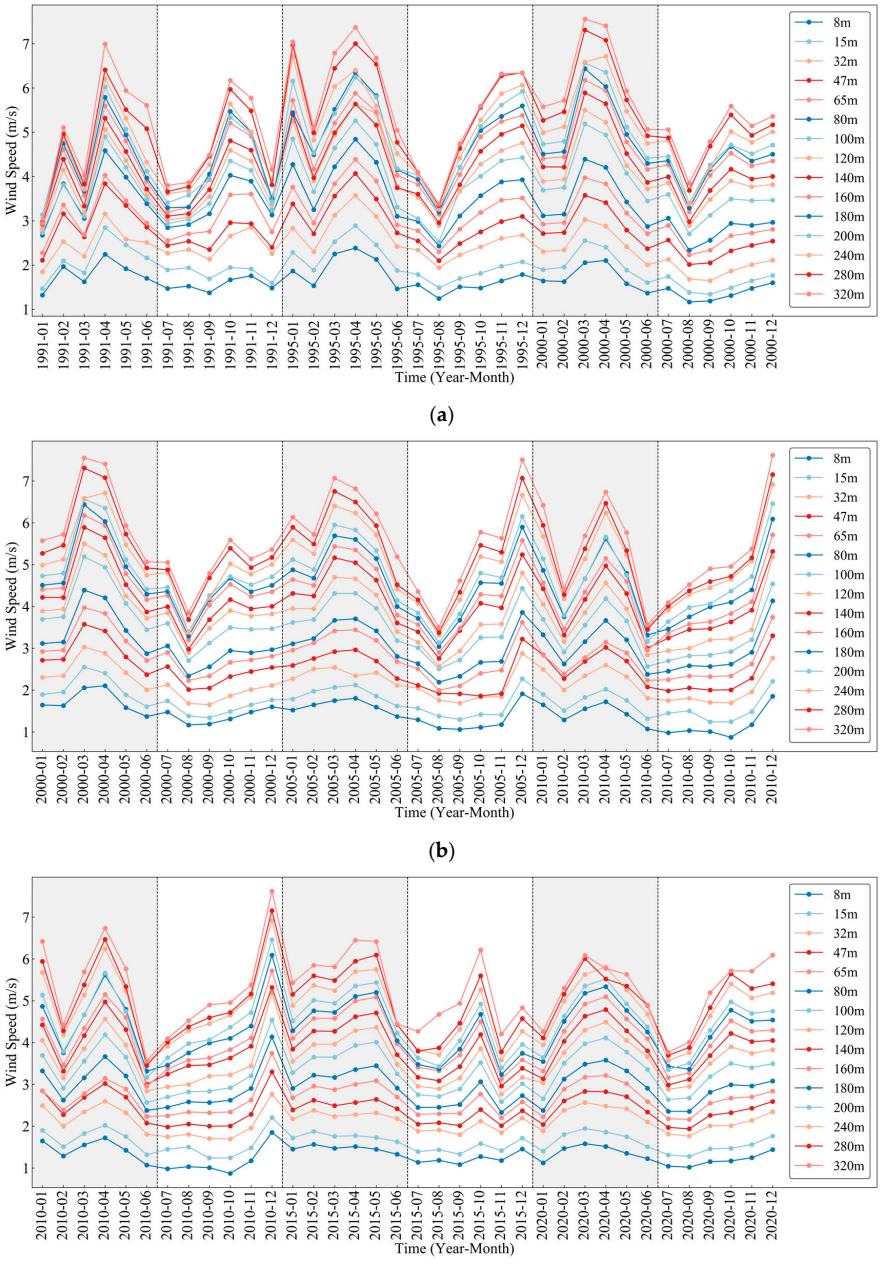
where k is the number of parameters in the model, n is the number of data points, and L is the maximum likelihood estimate of the model (the value of the likelihood function for the observed data under the optimal parameters).

The foundation of AIC is the concept of information entropy, aimed at minimizing the information loss between the true distribution and the model distribution. It focuses on finding the model that fits the data best while penalizing an increase in the number of model parameters. BIC is a model selection criterion based on the likelihood function, derived from Bayesian principles. It imposes a stricter penalty on the number of parameters than AIC and places more emphasis on finding the model most likely to generate the observed data from the true process [45,46].

3. Results

3.1. Time Series Analysis of Wind Speed at Different Heights

In the comprehensive analysis of wind speed data from 1991 to 2020, considering the diverse trends in wind speed changes across different periods, the timeline was divided into three distinct intervals: 1991 to 2000, 2000 to 2010, and 2010 to 2020. Additionally, recognizing the influence of varying altitudes on wind speed variations, these were classified into three primary strata: lower level (8 m to 47 m), middle level (65 m to 140 m), and upper level (160 m to 320 m). During the 1991 to 2000 interval, the average wind speed at the lower level saw a decrease of approximately 0.18 m/s, while the wind speeds at the middle and upper levels increased from 3.56 m/s and 4.45 m/s to 3.62 m/s and 5.01 m/s, respectively, showing growth rates of about 1.69% and 12.58%, as shown in Figure 4a.



(**a**)

(**b**)

(**c**)

Figure 4. Monthly average wind speed trends at various altitudes from 1991 to 2020. (**a**) Monthly average wind speed changes from 1991 to 2000. (**b**) Monthly average wind speed changes from 2000 to 2010. (**c**) Monthly average wind speed changes from 2010 to 2020.

Over the decade from 2000 to 2010, a decrease in wind speeds was noted across all altitude strata. At the lower level, the wind speed fell from 2.05 m/s in 2000 to 1.87 m/s in 2010, a reduction of about 8.78%. For the middle level, the wind speed decreased from 3.62 m/s in 2000 to 3.29 m/s in 2010, roughly a 9.12% decline. At the upper level, the wind speed dropped from 5.01 m/s in 2000 to 4.73 m/s in 2010, a decrease of approximately 5.99%. Contrary to the previous decade, this period observed a declining trend in wind speeds at the middle and upper levels, as shown in Figure 4b.

Between 2010 and 2020, the wind speeds at all levels remained largely stable, with only slight variations. At the lower level, the wind speed marginally decreased from 1.87 m/s in 2010 to 1.86 m/s in 2020, a decline of about 0.53%. At the middle level, there was a minor increase in the wind speed from 3.29 m/s in 2010 to 3.31 m/s in 2020, an increase of approximately 0.61%. At the upper level, the wind speed slightly fell from 4.73 m/s in 2010 to 4.67 m/s in 2020, a decrease of around 1.27%. Similarly, the consistent seasonal pattern was observed across all strata, as shown in Figure 4c.

Overall, throughout the entire 30 years, the wind speed at the lower level showed a declining trend, with an overall average decrease of 16.59%, with the most significant reduction occurring in the first two decades. The primary factors for this decline likely include an increase in surface roughness due to urbanization. The wind speeds at the middle and upper levels experienced a decline after 1995 but saw a resurgence in 2015. Overall, the wind speed at the middle level decreased by about 7.02%, while at the upper level, it inversely increased by about 4.94%. These changes suggest that although the wind speeds at the middle and upper levels are affected by the urban substrate, this influence is relatively weak, and they are more likely influenced by factors related to global climate change. Table 2 shows the average wind speeds at different altitude levels for each year from 1991 to 2020. Table 3 shows the statistical measures of wind speed samples at various heights.

Table 2. Average wind speeds at different altitude levels from 1991 to 2020.

Y_n	L (m/s)	M (m/s)	U (m/s)
1991	2.23	3.56	4.45
1995	2.36	3.98	5.21
2000	2.05	3.62	5.01
2005	1.95	3.46	5.02
2010	1.87	3.29	4.73
2015	1.85	3.23	4.60
2020	1.86	3.31	4.67

Y_n—number of years; L—average wind speeds at the lower level; M—average wind speeds at the middle level; U—average wind speeds at the upper level.

Table 3. Summary of wind speed statistics at different heights from 1991 to 2020.

Height	Maximum	Mean	SD	Range	IQR	Skewness	Kurtosis
8 m	11.2	1.463	0.950	11.1	0.8	2.015	5.445
15 m	11.5	1.762	1.106	11.4	1.1	2.021	5.254
32 m	13.7	2.252	1.350	13.5	1.3	1.881	4.527
47 m	16.1	2.567	1.586	15.9	1.6	1.783	4.060
65 m	16.9	2.873	1.735	16.7	1.9	1.646	3.509
80 m	18.5	3.158	1.957	18.3	2.2	1.587	3.102
100 m	19.0	3.565	2.202	18.8	2.7	1.389	2.242
120 m	19.5	3.852	2.401	19.4	2.9	1.291	1.902
140 m	21.3	4.100	2.584	21.2	3.3	1.225	1.557
160 m	23.1	4.344	2.757	23.0	3.6	1.152	1.287
180 m	23.6	4.530	2.902	23.4	3.8	1.107	1.135
200 m	24.9	4.683	3.020	24.7	4.1	1.077	0.978
240 m	23.4	4.973	3.254	23.2	4.4	1.045	0.807
280 m	26.2	5.206	3.448	26.0	4.7	1.041	0.767
320 m	26.5	5.471	3.638	26.3	5.0	1.014	0.666

SD—standard deviation; range—the difference between the maximum value and the minimum value; IQR—interquartile range.

From Table 3, it can be observed that the average wind speed increases with height, which can be attributed to the decreasing influence of surface friction on wind speed as the height increases. Simultaneously, with increasing height, the standard deviation and range of wind speed also increase, indicating a greater variability and uncertainty in wind speed in higher-altitude regions, implying an increased complexity in the influences of various atmospheric processes on high-altitude wind fields. The gradual decrease in skewness and the decline in kurtosis reflect a transition in wind speed distribution from a distinct positive skewness to a more symmetric shape from low to high speeds. This transition in distribution shape may be related to the dynamic characteristics of atmospheric stratification and vertical airflow, where the diffusion of wind speed extremes diminishes at higher altitudes, leading to an overall trend towards a normal distribution.

When conducting an overall trend analysis using monthly average wind speeds, we observed significant seasonal characteristics in the annual changes in wind speeds. However, these seasonal characteristics are cyclical, with wind speeds experiencing significant fluctuations during different periods of the year. Using annual averages does not effectively quantify the trends in wind speed changes at the quarterly level. To better investigate the variation in wind speed at different altitudes in different seasons, we classified the wind speed into four seasons, namely, spring, summer, autumn, and winter, as shown in Figure 5.

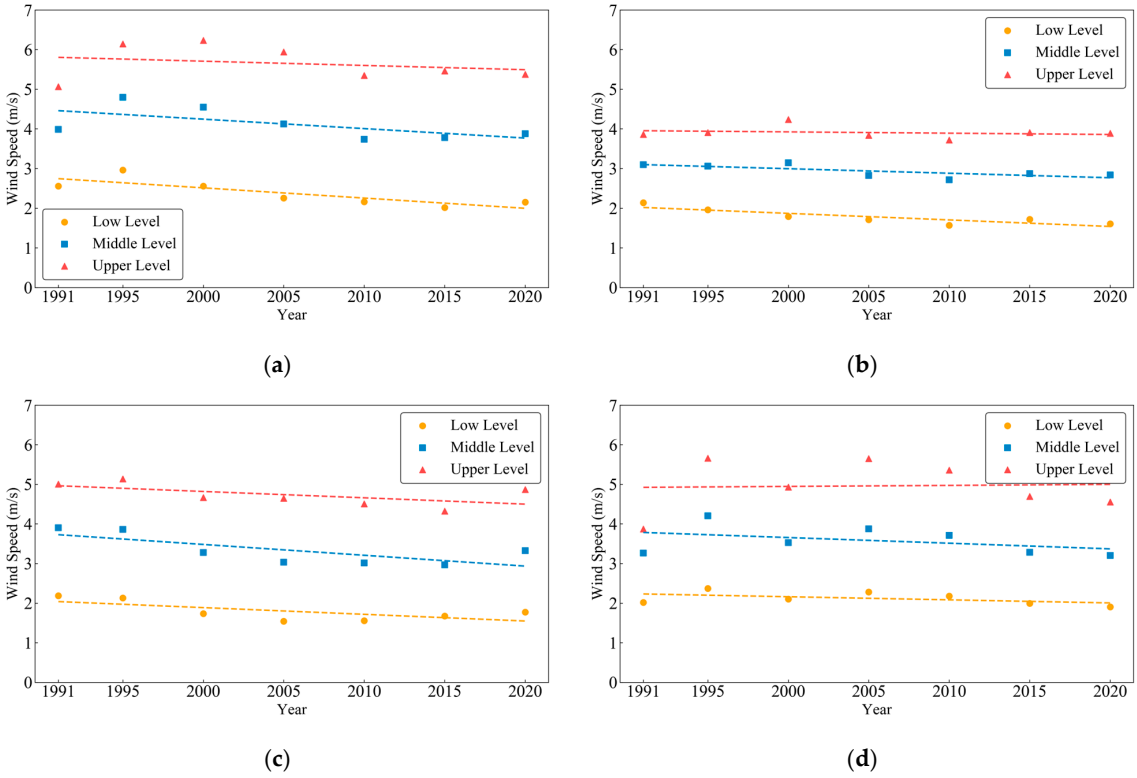


Figure 5. Changes in average wind speed at different altitude levels in different seasons. (**a**) Average wind speed in spring. (**b**) Average wind speed in summer. (**c**) Average wind speed in autumn. (**d**) Average wind speed in winter.

The least squares analysis of linear regression models over the past three decades reveals a predominantly downward trend in wind speeds across most seasons and altitudes. Notably, in spring, the decline is particularly pronounced at the lower and middle levels, with model slopes of 0.0258 and 0.0238, respectively, indicating significant velocity decreases. In contrast, the upper level exhibits a milder reduction with a slope of 0.0107 (Figure 5a). During summer, wind speed fluctuations are relatively stable but still show an overall decline (Figure 5b). Autumn presents the most substantial decrease at the middle level, with a slope of 0.0274, while both the lower and upper levels also show noticeable

declines, with slopes of 0.0169 and 0.0160, respectively, confirming a uniform reduction across all levels (Figure 5c). Winter, however, sees a slight increase in wind speed at the upper level, with a slope of 0.0025, whereas the lower and middle levels continue a mild downward trend, with slopes of 0.0078 and 0.0143, respectively (Figure 5d). Collectively, these patterns highlight that reductions in wind speeds are most significant in spring and autumn at the lower and middle levels, while summer exhibits relatively stable yet lower wind speeds. Integrating these data with monthly trends, it becomes evident that despite annual increases in spring and winter, there is a long-term downward trend in wind speeds across all seasons, including summer. The slight winter increase at the upper level may be attributed to inherently higher wind speeds and greater variability at this altitude. Table 4 details the fitting functions for different height levels across seasons.

Table 4. Fitting functions for different altitude levels in different seasons.

S_n	RE_l	RE_m	RE_u
Spring	y = 54.03 − 0.0258x	y = 51.85 − 0.0238x	y = 21.16 − 0.0107x
Summer	y = 34.92 − 0.0165x	y = 25.85 − 0.0114x	y = 10.49 − 0.0033x
Autumn	y = 35.73 − 0.0169x	y = 58.19 − 0.0274x	y = 36.80 − 0.0160x
Winter	y = 17.78 − 0.0078x	y = 32.23 − 0.0143x	y = −0.15 + 0.0025x

RE_l—low-level regression equations; RE_m—middle-level regression equations; RE_u—upper-level regression equations.

To study the trend of wind speed changes among various altitudes, we use Power Law Wind Profile Theory to describe the relationship between different altitude levels. Power Law Wind Profile Theory is a common method used in wind engineering to express the relationship between wind speed and altitude, as shown in Equation (1). The magnitude of the α value reflects the rate of increase in wind speed with altitude. We use the least squares method to fit the data. Since the calculation process of the optimal parameter values is quite dependent on the initial parameter values due to its nonlinearity, we transform Equation (1) into a linear model, Equation (13), through logarithmic change:

$$logv(z) = logv\left(z_{ref}\right) + \alpha log\left(\frac{z}{z_{ref}}\right) \tag{13}$$

Subsequently, we fit the average wind speed for each month, calculating the optimal α value for each month. Taking January 2000 as an example, we visualize the original height and wind speed scale to demonstrate the actual nonlinear relationship, as shown in Figure 6.

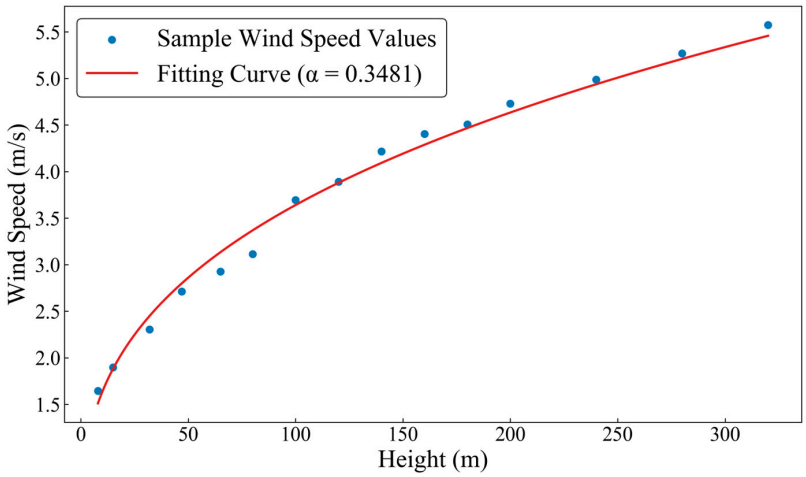


Figure 6. Optimal fitting of the wind shear index α for monthly average wind speed: an example from January 2000.

Using the least squares method and Mann–Kendall trend analysis, we examined monthly wind shear index values in Beijing over the past 30 years. Both methods revealed a statistically significant upward trend. Specifically, the least squares analysis showed an average annual increase of 0.003 in the wind shear index, and the Mann–Kendall analysis yielded a Z value of 5.617. This trend could be influenced by factors such as climate change, atmospheric circulation changes, and human activities. Increased wind shear might affect atmospheric stability, potentially causing instability when warm, moist air interacts with swiftly moving upper cold air. This could increase convective activities and the likelihood of extreme weather events like thunderstorms and heavy precipitation. Furthermore, a higher wind shear index could enhance vertical mixing, helping transport ground-level pollutants to higher altitudes and impacting weather patterns and climate, as shown in Figure 7.

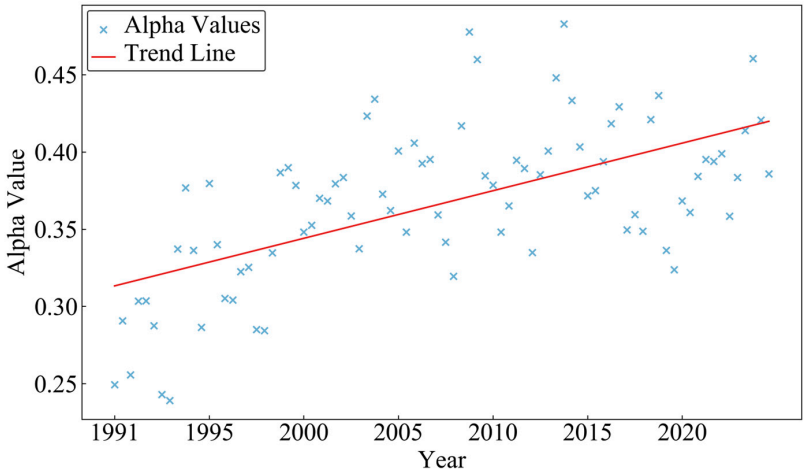


Figure 7. Time series of α values from 1991 to 2020 with trend line.

After obtaining the optimal α value for each month, the wind speed is adjusted to the standard statistical height (10 m) specified in the regulations. When calculating the basic wind speed, the maximum wind speed value in the time sequence segment is used. The maximum wind speed for each month is obtained through maximum value sampling, and then compared with the monthly average time series for trend analysis, as shown in Figure 8.

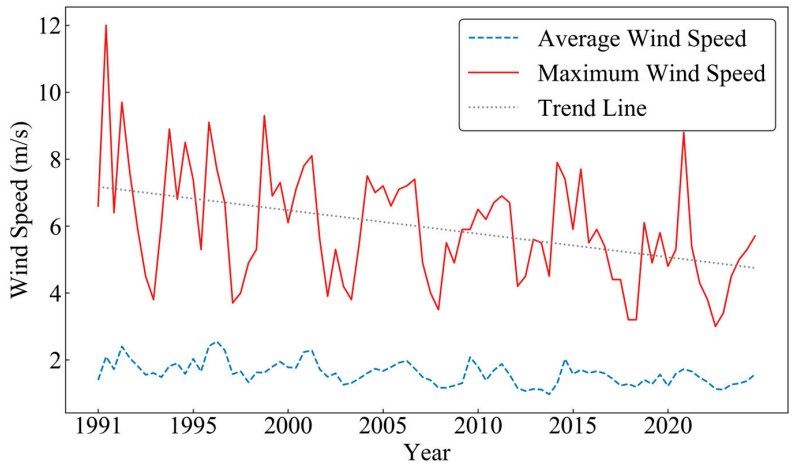


Figure 8. Overall trend of wind speed at 10 m height.

From the trend line, the change trend of the maximum wind speed is like that of the overall average wind speed, and it also shows a downward trend (Z value is −3.71, p value is less than 0.05). The maximum wind speed has more pronounced seasonal fluctuation

characteristics compared to the average wind speed. To more visually demonstrate this characteristic, the maximum wind speed is integrated into a monthly scale for fitting, as shown in Figure 9.

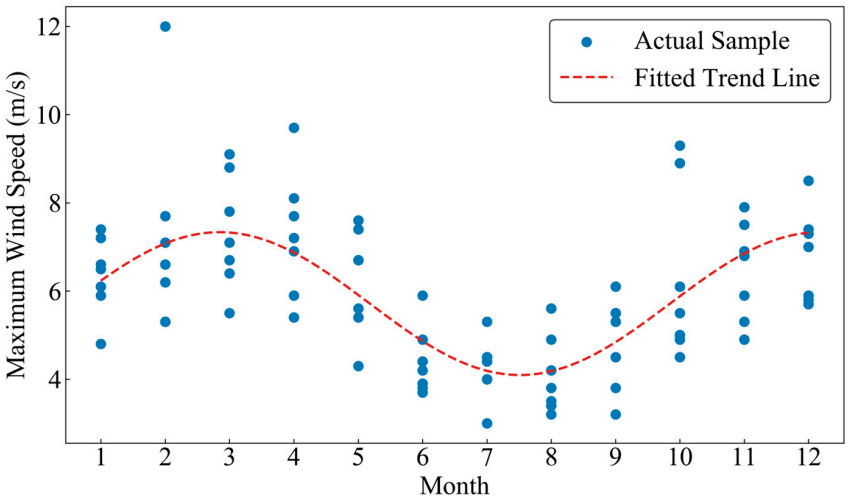
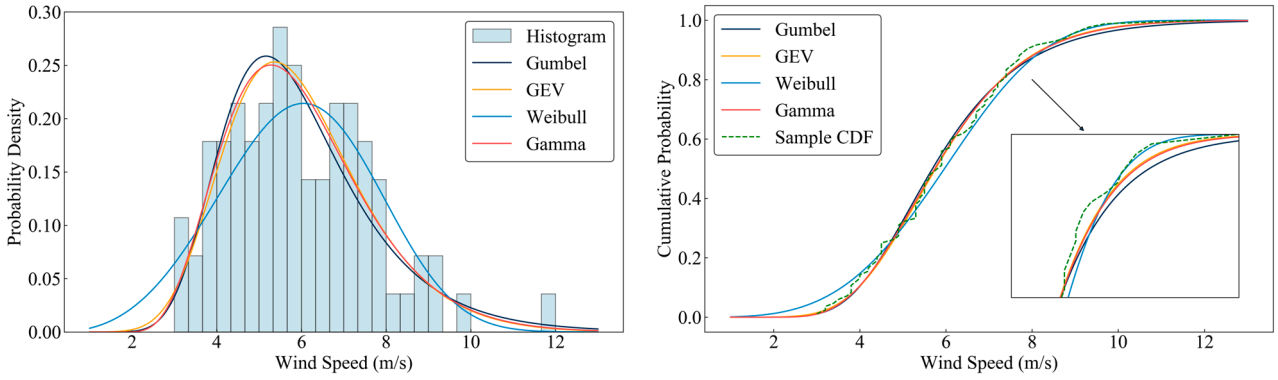


Figure 9. Seasonal trends in wind speed at 10 m height.

Maximum wind speed is significantly affected by seasonal factors, with peaks mainly occurring in winter and early spring. In the seasonal trend fitting, only a sine function was initially used for analysis. However, the results show that the variability of maximum wind speed is high. In subsequent model development, consideration is given to using more complex functions to capture its variability characteristics (see Section 3.2 for details).

3.2. Development and Evaluation of Wind Speed Models

The primary step in calculating the basic wind speed is to select an appropriate probability distribution model. We have chosen four common distribution models often used in extreme value theory and risk analysis, namely the Gumbel model (Type I extreme value), the Weibull model (in its two-parameter form), the GEV model, and the Gamma model. These four models are compared. Figure 10 illustrates the fit between the probability histogram of maximum wind speed and the probability density functions of the four models, as well as the fit between the cumulative distribution functions of the four models and the wind speed samples.



(**a**) (**b**)

Figure 10. The comparison of fitting situations among the four models. (**a**) Probability density function (PDF). (**b**) Cumulative distribution function (CDF).

From Figure 10a, it can be observed that the Gamma distribution matches the observed data best in the mid-range wind speed region, but its fit is poor in the high wind speed region. The Weibull distribution performs well in the mid-to-low wind speed range but exhibits slight deviations in the high wind speed tail. Both the Gumbel and GEV distributions fit closely throughout the entire wind speed range, particularly matching the actual data well in the tail. Figure 10b demonstrates that, apart from minor differences in the front and middle parts for the Weibull distribution, the estimates of non-extreme wind speed values from the other three distributions are close. In the extreme event probability section, the GEV and Gamma distributions closely resemble the sample CDF, possibly due to their flexibility and capability to model extreme values.

Apart from the visual results, it is also necessary to consider the evaluation metrics of the four distributions to assess the optimal model among them. Table 5 provides the evaluation values of the four models under four testing methods.

Table 5. Results of the test on four maximum wind speed distribution models.

M_n	NLL	AIC	BIC	K-S(D-*p*)
Gumbel	160.596	325.191	330.053	0.081–0.606
GEV	160.038	326.077	333.369	0.063–0.869
Weibull	164.394	334.787	342.080	0.073–0.730
Gamma	159.686	325.371	332.664	0.070–0.769

K-S(D-*p*)—Kolmogorov–Smirnov test results, where D is the test statistic and *p* is the *p*-value.

Based on the results, the Gumbel model fits best according to the AIC and BIC tests, with the lowest AIC and BIC values. Apart from the standard Weibull model, the other three distributions have very similar indicators, all of which are lower than those of the Weibull model. In the results for the negative log-likelihood (NLL), the best fit is the Gamma model (159.686), closely followed by the GEV model (160.038). In the K-S test, the GEV distribution fits best with the smallest D statistic (0.063) among all distributions, indicating that the sample distribution is very close to the reference distribution, and with the highest *p*-value (0.869), suggesting no significant difference between the sample data and the assumed distribution. Considering the flexibility of the GEV model and its theoretical foundation in extreme value theory, we choose the GEV distribution (generalized extreme value distribution) as the optimal model for the steady state.

In most studies, when using the GEV model, the location, scale, and shape parameters (μ, σ, and ξ) are considered constants, not changing over time or with other variables, i.e., a stationary GEV model, if the probability distribution of extreme events does not change over time, and the risks in the past, present, and future is the same. However, in the trend analysis in the previous section, we found that the wind speed shows significant changes on monthly, quarterly, and annual scales. Therefore, we adopted a non-stationary GEV model, if the probability distribution of the maximum wind speed changes over time, allowing the location, scale, and shape parameters to change over time. The parameters were modeled as functions dependent on time, with the expectation that the model can more flexibly adapt to environmental or climate changes.

In the research conducted by previous scholars, it was discovered that allowing the shape parameter to vary could lead to computational problems [47]. Therefore, we consider first introducing a time-varying function for the location parameter and, on this basis, introducing a time-varying function for the location parameter. Then, we compare and evaluate the stationary GEV model with these two non-stationary models. Regarding the location parameter, combining the results of the long-term trend analysis from the previous section, we first introduce a linear function, as shown in Equation (14):

$$\mu(t) = \beta_0 + \beta_1 \cdot T \tag{14}$$

where $\mu(t)$ is the location parameter at time t, T is the time variable, β_0 is the base location parameter, and β_1 is the coefficient related to the time variable. Meanwhile, due to the appar-

ent seasonal characteristics of the wind speed throughout the entire time series (as shown in Figure 9), to capture this periodic feature, we decompose the potentially existing periodic functions into a sum of sine and cosine functions using Fourier series. We set the month as the periodic variable, M, and combine it with Equation (14) to obtain Equation (15):

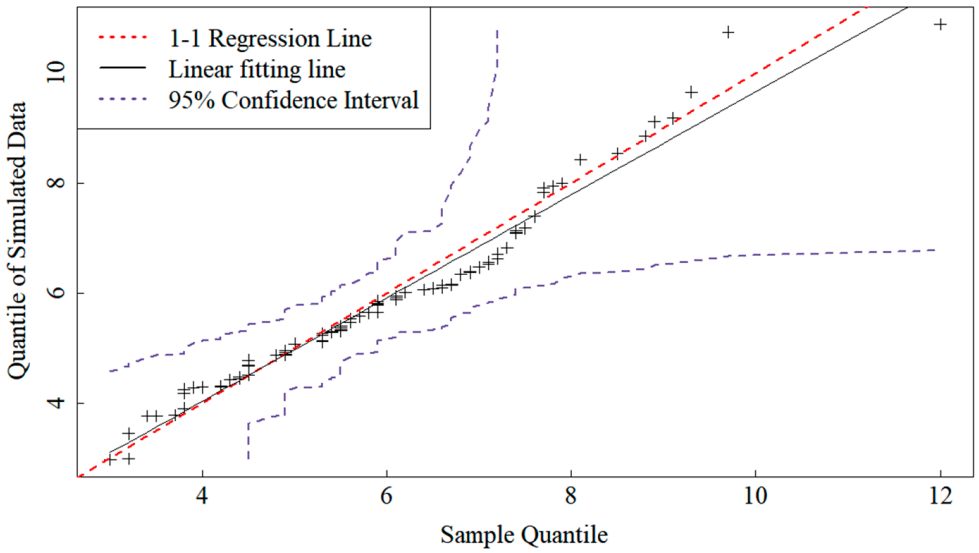
$$\mu(t) = \beta_0 + \beta_1 \cdot T + \beta_2 \cdot cos\left(\frac{2\pi \cdot M}{12}\right) + \beta_3 \cdot sin\left(\frac{2\pi \cdot M}{12}\right) \quad (15)$$

where β_2 and β_3 are the coefficients related to the cosine and sine terms, and M is the value of the month.

For the scale parameter, we introduce a function identical to the function for the location parameter. Research indicates that, since the scale parameter must be positive, the scale parameter is set using the logarithmic form [48]. However, setting parameters in logarithmic form makes the interpretation of parameters in the results more complex and requires the re-transformation to calculate the corresponding estimated values. We use the "extRemes" package in R to perform a simulation of non-stationary GEV, where the scale parameter is set to positive values by default [49], so the form of the function does not change, as shown in Equation (16):

$$\sigma(t) = \gamma_0 + \gamma_1 \cdot T + \gamma_2 \cdot cos\left(\frac{2\pi \cdot M}{12}\right) + \gamma_3 \cdot sin\left(\frac{2\pi \cdot M}{12}\right) \quad (16)$$

where the meaning of the parameters is consistent with Equation (15). After obtaining the best fit parameters through Maximum Likelihood Estimation (MLE), we compared the stationary GEV distribution with two types of non-stationary GEV distributions (considering only the variation in the location parameter and considering the variations in both the location and scale parameters). First, we compared the quantiles between the actual data and the model-predicted data, as shown in Figure 11.



(a)

Figure 11. *Cont.*

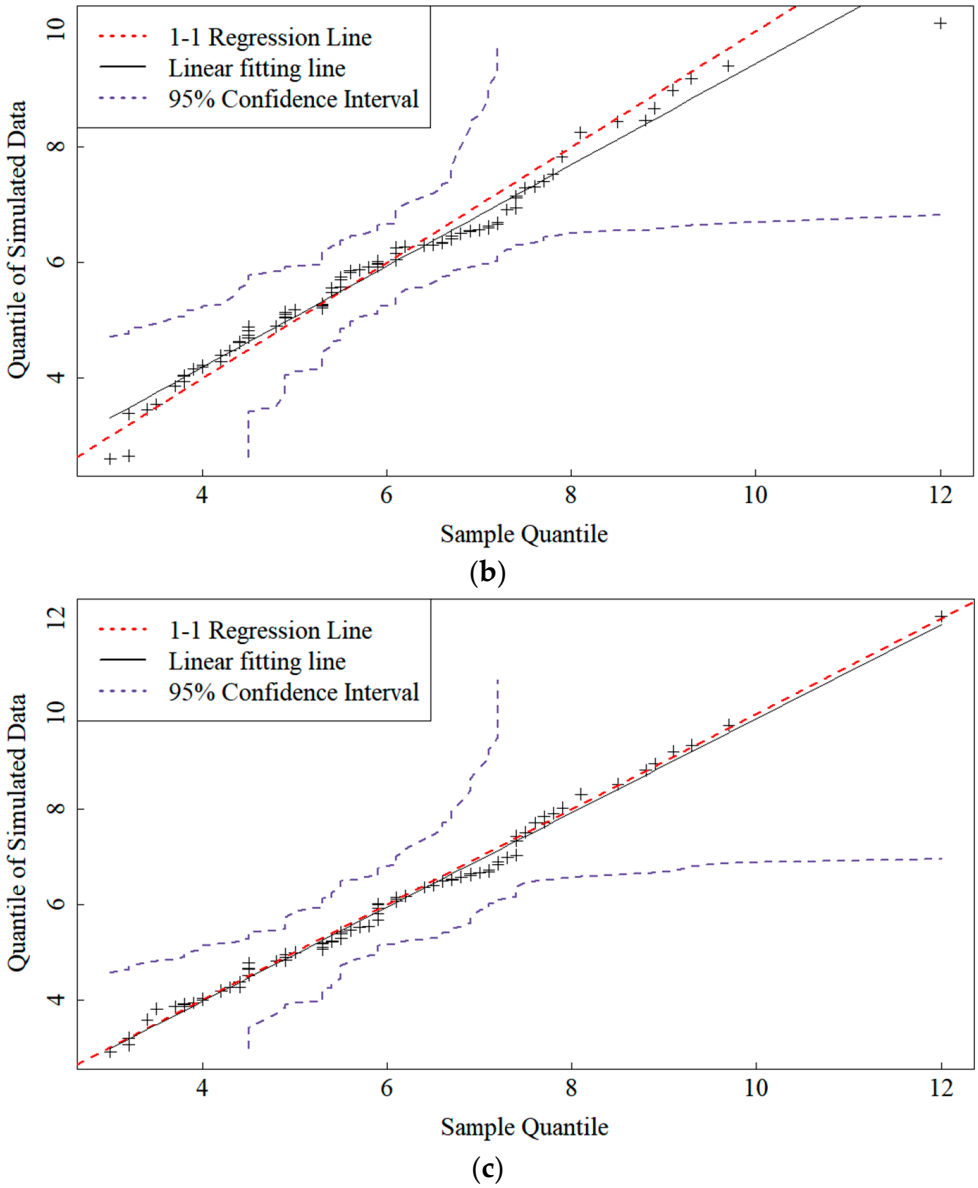


Figure 11. Quantile–quantile plots of the three generalized extreme value models. (**a**) The stationary GEV model. (**b**) The non-stationary GEV model with variation in the location parameter. (**c**) The non-stationary GEV model with variations in both the location and scale parameters.

In Figure 11, the horizontal axis represents quantiles from actual samples, while the vertical axis represents quantiles predicted by the theoretical distribution of the model. In theory, if the samples perfectly match the theoretical distribution, data points should fall on the reference line labeled "1-1 line". The solid line represents the fit between sample quantiles and theoretical quantiles; if actual data closely match the model data, this line will be very close to the "1-1 line". The dashed line represents the 95% confidence interval of the regression line. If this interval includes the "1-1 line", it typically indicates acceptable model-data matching.

In the stationary GEV model, most points cluster near the reference line, indicating general consistency between actual samples and the model. However, at the middle and high quantiles on the horizontal axis, data points begin to deviate from the reference line, indicating less accurate predictions in these areas. In the non-stationary GEV model considering variations in the location parameter over time, overall data points still cluster near the reference line. Although its performance at middle quantiles is better than the stationary GEV model, its fit line begins to deviate from the reference line at high quantiles,

even more so than the stationary GEV distribution. In the GEV model considering changes in both location and scale parameters, the reference line and fit line become very close, indicating the better capture of extreme value characteristics and closer agreement between predicted and sample quantiles.

While visual results allow for intuitive assessment, specific model evaluation requires numerical analysis in addition to visualization. Employing the same evaluation methods as before (excluding K-S due to its inability to reflect dynamism), specific evaluation values are shown in Table 6.

Table 6. Comprehensive evaluation results of the three GEV models.

G_n	NLL	AIC	BIC
GEV	160.038	326.077	333.369
GEV_{n1}	127.400	266.799	281.384
GEV_{n2}	120.380	258.760	280.637

GEV—stationary GEV model; GEV_{n1}—non-stationary GEV model with variation in location parameter; GEV_{n2}—non-stationary GEV model with variations in both location and scale parameters.

The results from Table 6 indicate that, in terms of NLL values, the GEVn2 model (NLL = 120.380) demonstrates the best fit, followed by the GEVn1 model (NLL = 127.400), while the stationary GEV model (NLL = 160.038) exhibits the lowest fit.

Introducing a function of time variables into the stationary GEV model noticeably enhances the overall model performance. Upon incorporating changes in the scale parameters over time, following the variation in location parameters, the reduction in the model's NLL value is marginal, merely improving some predictive capabilities. Due to the increased number of parameters, both AIC and BIC values are simultaneously employed for comprehensive evaluation to prevent the decrease in NLL values attributed to overfitting. It is evident that the GEVn2 model continues to perform the best (AIC = 258.760, BIC = 280.637), with the GEVn1 model (AIC = 266.799, BIC = 281.384) still outperforming the stationary GEV model (AIC = 326.077, BIC = 333.369).

AIC and BIC values strike a balance between model complexity and fit. Integrating visual results, it is concluded that the non-stationary GEV model considering simultaneous variations in location and scale parameters outperforms the other two models. Parameters for the three GEV models are presented in Table 7.

Table 7. Parameter estimates for stationary and non-stationary GEV models.

G_n	μ	σ	ξ	β_0	β_1	β_2	β_3	γ_0	γ_1	γ_2	γ_3
GEV	5.234	1.459	0.088	-	-	-	-	-	-	-	-
GEV_{n1}	-	0.963	0.038	6.191	−0.018	0.853	0.922	-	-	-	-
GEV_{n2}	-	-	0.081	6.396	−0.021	0.948	1.070	1.352	−0.009	0.237	0.118

μ—the location parameter; σ—the scale parameter; ξ—the shape parameter. Additional parameters are detailed in Equations (15) and (16).

3.3. Evaluation of Basic Wind Speed and Wind Pressure Height Variation Coefficients

In traditional stationary models, we can calculate the corresponding event intensity for a given return period, and these return levels are standard. Taking the stationary GEV distribution model as an example, as shown in Figure 12, the horizontal axis represents the return period, and the vertical axis represents the standard return level (wind speed value) corresponding to that return period, with the solid line being the fitted return line. As the return period increases, the corresponding return level becomes greater, and the uncertainty also increases, but this change does not vary over time. We refer to it as the standard return level.

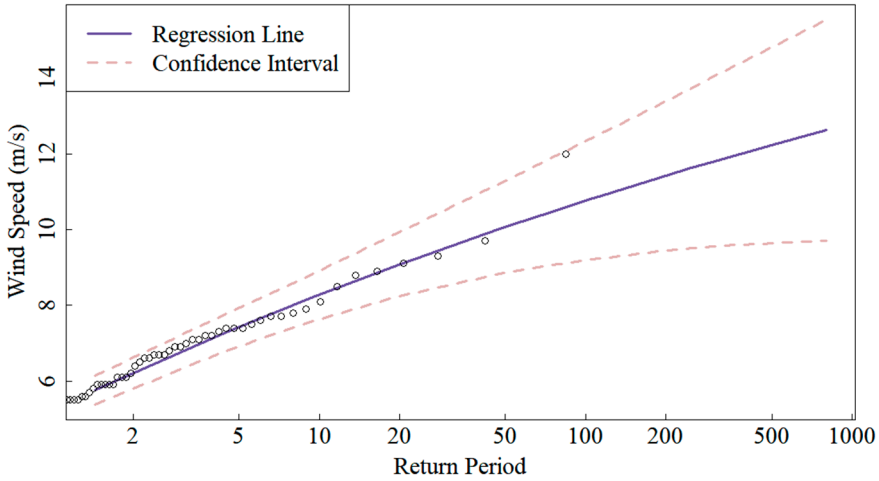


Figure 12. Standard return level plot for the stationary GEV model.

However, due to the impact of climate change and other non-static factors, the standard return levels may no longer be accurate. Effective return levels consider factors that change over time, allowing return levels to change over time while keeping the probability of the event occurring constantly. This means that, over time, even though the physical level of the event (such as wind speed) changes, the probability of the same risk occurring remains unchanged [50], as shown in Figure 13.

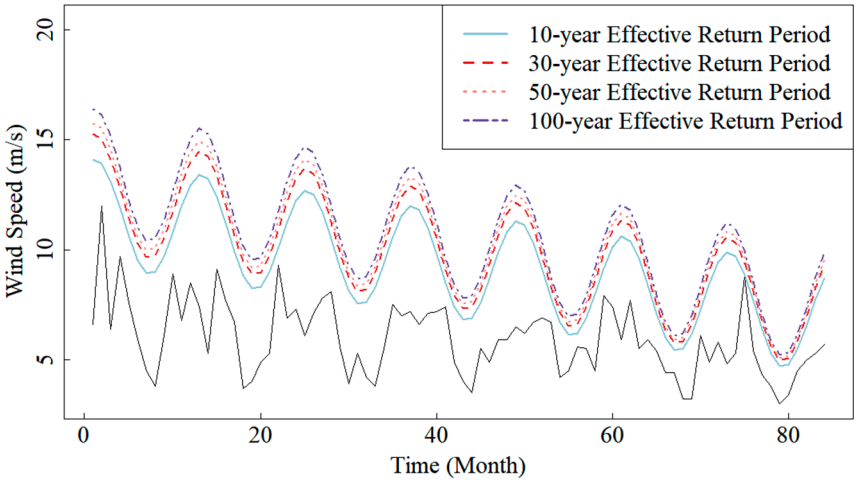


Figure 13. Effective return level plot for non-stationary GEV model variations in both location and scale parameters.

In the figure, the effective return level plot takes time points as the horizontal axis and uses different curves to depict different return periods. The black line represents the maximum wind speed that fluctuates over time. It adjusts the risk levels at different time points to reflect changes over time. However, considering the uncertainty of the data and potential future trends, when using effective return levels to make risk assessments, specific practical applications and focal points need to be considered. When setting design standards, to ensure safety under extreme conditions, we generally choose the least favorable conditions' effective level for calculation. In this study, we select the maximum value among the effective return levels as the basic wind speed for a specific return period, and we compare the results with those calculated using the stationary GEV model and China's "Load Code for the Design of Building Structures" GB50009-2012 [51]. The comparison is shown in Figure 14 and Table 8.

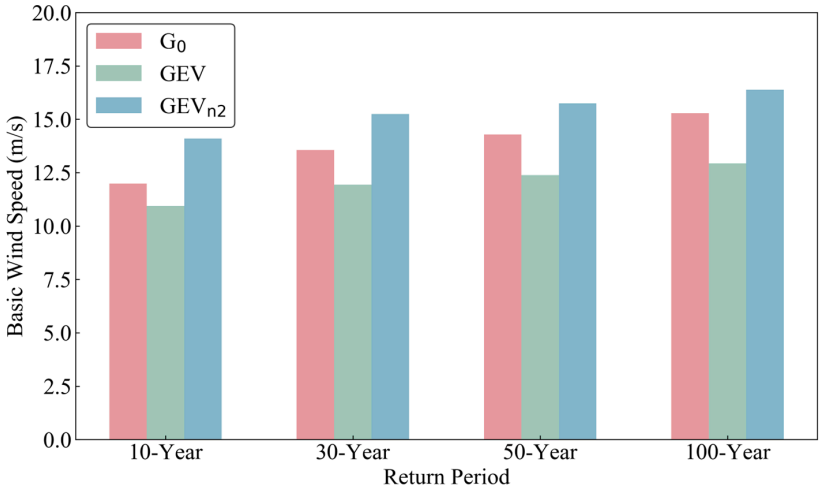


Figure 14. Comparison of basic wind speed values obtained by different calculation methods under different recurrence periods.

Table 8. Basic wind speed values of different models under various return periods.

G_n	10-RP (m/s)	30-RP (m/s)	50-RP (m/s)	100-RP (m/s)
G_0	11.99	13.56	14.29	15.28
GEV	10.94	11.94	12.38	12.94
GEV_{n2}	14.10	15.25	15.75	16.39

G_0—model used in the standard; RP—basic wind speed for a specific return period.

From the results, it can be observed that the basic wind speeds calculated by the stationary GEV model for all return periods are lower than the calculated values in the standards. The results from the QQ plots in the previous section indicate that its capturing capability for the maximum wind speeds at medium to high quantiles is not excellent. In the GEV2 model, which simultaneously considers changes in both location and scale parameters, the calculated basic wind speeds overall exceed those calculated in the standards. Only at higher return periods do the values become relatively close (15.28–16.39). This might be attributed to its capture of more extreme values in the time series, where the dynamic return levels provide a more stable benchmark for risk assessment, indicating that the basic wind speed values calculated by the standards over long time series may be underestimated without considering trend effects.

The basic wind speed values are obtained after adjusting the maximum wind speed to a height of 10 m. However, the wind profile analysis in Section 3.1 indicates that the relationship between wind speeds at different heights also varies over time (wind profile indices show an increasing trend). In the standard [51], calculating the design wind load for specific heights uses fixed wind pressure height variation coefficients. For terrain features categorized as Class C and Class D (urban terrain features defined in the standards [51]), the empirical formulas for wind pressure height variation coefficients are, respectively, given by Equation (17):

$$\begin{cases} \mu^C = 0.544\left(\frac{z}{10}\right)^{0.44} \\ \mu^D = 0.262\left(\frac{z}{10}\right)^{0.60} \end{cases} \quad (17)$$

where μ^C represents the wind pressure height variation coefficient for Class C terrain features, μ^D represents the wind pressure height variation coefficient for Class D terrain features, z corresponds to the height value, and the empirical coefficients 0.544 and 0.262, respectively, represent the surface roughness coefficients. The formulas are derived based on wind profile equations and wind pressure calculation formulas, and the specific derivation process is not elaborated here. The basic principle is to compare the wind pressure values at different heights with the basic wind pressure values, while the air density value

is treated as a fixed value and canceled out in the fraction. The resulting empirical indices of 0.44 and 0.60 correspond to the wind profile indices for different terrain features (in the standards, the wind profile index for Class C terrain features is 0.22, and for Class D terrain features, it is 0.30, both raised to the power of 2α in the general formula).

Based on the optimal non-stationary GEV model and in conjunction with wind speed data from all 15 measured height layers, actual wind pressure values for each height layer can be obtained (assuming air density as a fixed value). Then, by calculating the basic wind pressure values from basic wind speed values, actual wind pressure height variation coefficients for the 15 height layers can be obtained. The wind pressure height variation coefficients in the standards provide values only for specific heights, but they can be converted to the heights used in the measured data in this paper using Equation (17). Since it is challenging to quantify ground roughness using measured data, actual values are computed using roughness indices identical to those specified in the standards for different terrain types, as shown in Table 9 (where the cutoff height for Class C terrain in the standards is 15 m and for Class D it is 30 m, meaning that wind pressure height variation coefficients below the cutoff height are taken at the position of the cutoff height, with an approximation for the 32 m height in Class D terrain to 30 m).

Table 9. Comparison of the wind pressure height variation coefficients between actual and standard values.

Height (m)	Class C Terrain Features	Class D Terrain Features
8	0.55 (0.65)	0.32 (0.51)
15	0.55 (0.65)	0.32 (0.51)
32	0.66 (0.91)	0.32 (0.53)
47	0.89 (1.08)	0.43 (0.66)
65	1.17 (1.24)	0.56 (0.81)
80	1.50 (1.36)	0.72 (0.91)
100	1.69 (1.50)	0.81 (1.04)
120	1.92 (1.62)	0.92 (1.16)
140	2.03 (1.74)	0.98 (1.28)
160	2.09 (1.84)	1.01 (1.38)
180	2.23 (1.94)	1.07 (1.48)
200	2.37 (2.03)	1.14 (1.58)
240	2.50 (2.20)	1.20 (1.76)
280	2.53 (2.36)	1.22 (1.94)
320	2.61 (2.50)	1.25 (2.10)

In parentheses are the values specified in the standards.

The wind pressure height variation coefficients for different terrain types are shown in Figure 15.

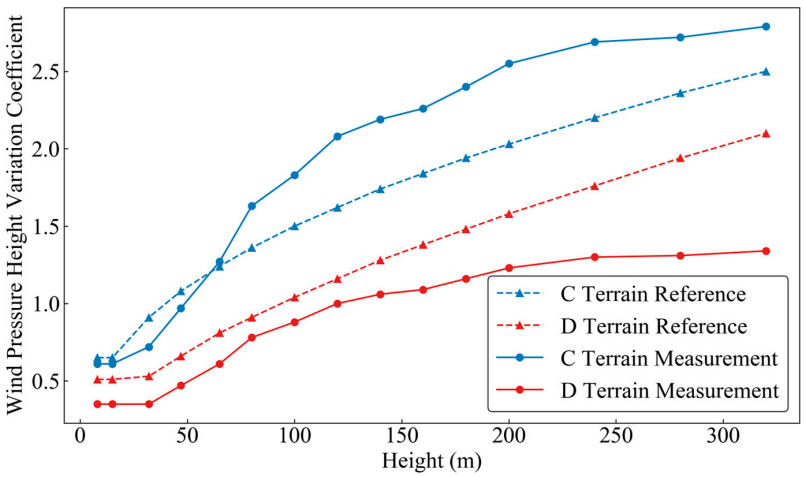


Figure 15. Comparison of measured wind pressure height variation coefficients with specifications for different terrain types.

The results indicate that, in Class C terrain features, the wind pressure height coefficients obtained from measurements and those specified in the standards are relatively close at lower heights. However, as the height increases, the wind pressure height variation coefficients obtained from measurements are significantly higher than those in Class C. For Class D terrain features, the wind pressure height variation coefficients specified in the standards are generally higher than those obtained from measurements. At lower heights, the difference between the two is relatively small, but as the height increases, the difference also increases. We believe that the wind pressure height variation coefficients for Beijing urban areas fall within the range specified in the standards for both Class C and Class D terrain features. At lower heights, they are closer to Class C values, while at higher heights, Class C underestimates the measured values, and Class D overestimates them.

4. Discussion

In the trend analysis of wind speed at different heights, we found that the overall trends of wind speeds at lower and upper levels are consistent, but the magnitudes are completely different. We believe that this is due to the impact of urbanization on surface winds. However, for the wind speeds at higher altitudes, the main reasons might be climate change and changes in atmospheric circulation patterns, which is consistent with the conclusions of many scholars [52–54]. Regarding the wind speed between different heights, we found that, although the overall wind speed shows a decreasing trend, the wind shear index shows an upward trend. For design standards, the wind speed near the ground (10 m) is generally used as the calculation value, where the fluctuation of such low-altitude observations will not be significant due to urbanization effects (as shown in Figure 6). However, the rise in the wind shear index means a decrease in atmospheric stability, which also leads to significant changes in the trend and magnitude of wind speed at higher altitudes. At this point, calculating wind loads through standards and empirical wind shear indices may not be accurate enough. This is a point that needs to be considered in the wind-resistant design of high-rise buildings, and it also provides some reference for the assessment of wind energy resources [55].

For this reason, we used a non-stationary GEV model to capture the distribution of extreme wind speeds under long-term changes as much as possible. Compared to previous studies [56,57], we also introduced a time-varying function into the scale parameter and used Fourier terms to capture seasonal characteristics. Among the obtained stationary and non-stationary models, the best-fitting model was selected for comparison with the basic wind speeds calculated through the standards, and it was considered that the values derived from the standards (which use stationary models and empirical data) are underestimated. At the same time, for Class D terrain features, a value of 0.3 was adopted as the wind profile exponent in the calculation formula for wind pressure height variation coefficients. Although Section 3.1 indicated that the overall level of the wind profile exponent is greater than 0.3, its focus was on mean wind speed. The samples used for calculating wind pressure height variation coefficients, however, represent maximum wind speeds. For wind speeds in the Beijing urban area, the influence of the boundary layer on low- and mid-level winds is significant, resulting in an overall lower average wind speed. However, the impact on higher-level winds is relatively small, and even exhibits an opposite trend, leading to a strong vertical average wind speed difference and thus yielding a higher wind profile exponent value. From the perspective of momentum transfer, it can be considered that the average wind speed observed over a longer period reflects the efficiency of momentum transfer throughout the entire atmospheric boundary layer more comprehensively. Over a longer period, momentum from lower altitudes in the atmosphere is more effectively transferred to higher levels, resulting in a significant increase in average wind speed with height.

In contrast, maximum wind speeds are obtained by sampling maximum values, which are typically associated with short-term strong winds. These strong winds may occur under specific meteorological conditions, where extreme wind speeds are often derived from

localized high-energy airflow and are limited in vertical diffusion. Therefore, the wind profile exponent value for maximum wind speeds tends to be smaller. If a value of 0.3 is adopted as the wind profile exponent and the maximum wind speed at 10 m height is 16 m/s, the calculated maximum wind speed at 320 m height would be close to 43 m/s, which is evidently an overestimation compared to the measured values in the sample.

Hence, the wind pressure height variation coefficients calculated based on Class D terrain features in the standards are relatively large. Similarly, for Class C terrain features, the measured values are close to the standard values at lower heights. This is partly because the atmosphere is more stable at lower altitudes, and wind speed variations are more uniform. Additionally, a wind profile exponent closer to the value used in the standards (0.22) indicates that the measured data at this height are more likely to approximate the long-term data based on Class C terrain features, as specified in the standards. However, extreme wind speeds measured at higher altitudes are accompanied by stronger turbulence and wind speed fluctuations, leading to relatively larger wind pressure height variation coefficients at higher altitudes compared to the Class C values specified in the standards.

The potential limitations of this article stem from the introduction of time-varying functions to the parameters, which means that conventional methods may amplify the impact of trends when calculating values for larger return periods, making it necessary to use effective return levels for interpretation. Furthermore, this paper introduces linear functions and periodic functions into the parameters to fit annual trends and seasonal trends. Subsequent research could consider using the variations of sine functions (sine waves with attenuation terms) to reconcile these two types of trends, or directly introduce other functions such as quadratic functions or piecewise functions to fit the more realistic and complex variations in actual data. Building on this, it could also explore calculating non-fixed air densities based on the joint distribution of wind speed and air density, or quantifying surface roughness to derive more accurate wind pressure height variation coefficients. Additionally, although the data span a large timeframe (fully experiencing urbanization), the years of the data are not continuous, with only representative years selected for analysis. Future research could use more covariates to more accurately estimate the changes in and the range of parameters, and they could also employ a more comprehensive data sample for more precise simulations.

5. Conclusions

This study conducts a long-term trend analysis of wind speeds at various heights in the urban areas of Beijing over the past 30 years. Building upon the optimal model, a non-stationary GEV model with time-varying functions is established. The obtained key parameters of design wind loads are compared and discussed in contrast to the standards. The main conclusions are as follows:

1. During the process of urbanization, the near-surface wind speed in the urban areas of Beijing has shown a decreasing trend over the past 30 years, while at higher altitudes, there has been a slight increasing trend. Apart from the winter high-altitude wind speeds, the wind speeds in all seasons generally exhibit a decreasing trend.
2. The trend of the wind shear index is inconsistent with the overall wind speed trend, showing an increasing trend. This promotes the dispersion of ground pollutants into the atmosphere and indicates that more extreme wind speed events occur at higher altitudes.
3. The overall evaluation metrics of the non-stationary GEV model are superior to those of the stationary GEV model. The introduction of time-varying functions enhances the model's predictive capabilities, albeit with a stricter penalty on the number of parameters shown by the BIC criterion.
4. The stationary GEV model performs poorly at higher quantiles, yielding basic wind speed values lower than the standards. The results of the model considering only changes in the location parameter closely match those of the standards, but incorpo-

rating changes in the scale parameter yields better evaluation metrics, suggesting that the standards underestimate basic wind speed values in this scenario.

5. In the urban areas of Beijing, the wind pressure height variation coefficients fall within the range specified for Class C and Class D terrain features in the standards. At lower heights, they closely resemble the values for Class C terrain features, while at higher heights, they exceed the values for Class C. The coefficients obtained using the calculation formula for Class D terrain features are generally higher than the measured wind pressure height variation coefficients.

Author Contributions: Conceptualization, X.J. and Z.Z.; Methodology, S.Y., X.J., Z.Z. and L.J.; Software, S.Y., Y.T., Z.Z. and L.J.; Validation, S.Y.; Formal analysis, X.J. and J.J.; Investigation, Y.T. and J.J.; Resources, X.J., Y.T. and J.J.; Data curation, S.Y., Y.T., J.J. and L.J.; Writing—original draft, S.Y.; Writing—review & editing, S.Y., X.J., Y.T., Z.Z. and L.J.; Visualization, S.Y.; Supervision, X.J.; Project administration, J.J.; Funding acquisition, X.J. All authors have read and agreed to the published version of the manuscript.

Funding: The investigation was supported by the National Natural Science Foundation of China (No. 31570708).

Data Availability Statement: The raw data supporting the conclusions of this article will be made available by the authors on request.

Conflicts of Interest: The authors declare no conflicts of interest.

References

1. Ali, M.M.; Al-Kodmany, K. Tall buildings and urban habitat of the 21st century: A global perspective. *Buildings* **2012**, *2*, 384–423. [CrossRef]
2. Škvorc, P.; Kozmar, H. Wind energy harnessing on tall buildings in urban environments. *Renew. Sustain. Energy Rev.* **2021**, *152*, 111662. [CrossRef]
3. Newman, R.; Noy, I. The global costs of extreme weather that are attributable to climate change. *Nat. Commun.* **2023**, *14*, 6103. [CrossRef] [PubMed]
4. Tang, L.; Liu, H.; Zheng, C. Effects of twisted wind flow on the mean wind load characteristics of super high-rise buildings with different heights. *J. Build. Eng.* **2023**, *75*, 106972. [CrossRef]
5. Liu, Y.; Xuan, C.; Xu, Y.; Fu, N.; Xiong, F.; Gan, L. Local climate effects of urban wind corridors in Beijing. *Urban Clim.* **2022**, *43*, 101181. [CrossRef]
6. Hong, H.; Tang, Q.; Yang, S.; Cui, X.; Cannon, A.; Lounis, Z.; Irwin, P. Calibration of the design wind load and snow load considering the historical climate statistics and climate change effects. *Struct. Saf.* **2021**, *93*, 102135. [CrossRef]
7. Ghazal, T.; Elshaer, A.; Aboshosha, H. Wind load evaluation on storm shelters using wind tunnel testing and North American design codes. *Eng. Struct.* **2022**, *254*, 113821. [CrossRef]
8. Iida, Y.; Uematsu, Y. Numerical study of wind loads on buildings induced by downbursts. *J. Wind. Eng. Ind. Aerodyn.* **2019**, *191*, 103–116. [CrossRef]
9. Zou, Q.; Li, Z.; Zou, F.; Zeng, X.; Wang, C.; Pan, Y. A study on the characteristics of roof wind field by wind tunnel test. *J. Build. Eng.* **2021**, *43*, 103155. [CrossRef]
10. Simiu, E.; Scanlan, R.H. *Wind Effects on Structures: Fundamentals and Applications to Design*; John Wiley: New York, NY, USA, 1996; Volume 688.
11. Li, Y.-G.; Liu, P.; Li, Y.; Yan, J.-H.; Quan, J. Wind loads characteristics of irregular shaped high-rise buildings. *Adv. Struct. Eng.* **2023**, *26*, 3–16. [CrossRef]
12. Yan, B.; Li, Q. Detached-eddy and large-eddy simulations of wind effects on a high-rise structure. *Comput. Fluids* **2017**, *150*, 74–83. [CrossRef]
13. Thordal, M.S.; Bennetsen, J.C.; Koss, H.H.H. Review for practical application of CFD for the determination of wind load on high-rise buildings. *J. Wind Eng. Ind. Aerodyn.* **2019**, *186*, 155–168. [CrossRef]
14. Fouad, N.S.; Mahmoud, G.H.; Nasr, N.E. Comparative study of international codes wind loads and CFD results for low rise buildings. *Alex. Eng. J.* **2018**, *57*, 3623–3639. [CrossRef]
15. Amiri, A.K.; Bucher, C. A procedure for in situ wind load reconstruction from structural response only based on field testing data. *J. Wind Eng. Ind. Aerodyn.* **2017**, *167*, 75–86. [CrossRef]
16. Li, R.; Wang, Y.; Lin, H.; Du, H.; Wang, C.; Chen, X.; Huang, M. A Mesoscale CFD Simulation Study of Basic Wind Pressure in Complex Terrain—A Case Study of Taizhou City. *Appl. Sci.* **2022**, *12*, 10481. [CrossRef]
17. Ye, T.; Zhu, L.; Tan, Z.; Li, L. Research on Wind Load Calculation Based on Identical Guarantee Rate Method. *Shock Vib.* **2021**, *2021*, 1831330. [CrossRef]

18. Suresh Kumar, K.; Rahul, P.; Li, S.; Gibbons, M. Revisiting basic wind speed of metro cities of India. *Nat. Hazards Rev.* **2021**, *22*. [CrossRef]
19. Chen, W.; Tian, Y. The Return Period Wind Speed Prediction of Beijing Urban Area Based on Short-Term Measured Wind Speed. *Atmosphere* **2024**, *15*, 159. [CrossRef]
20. Torrielli, A.; Repetto, M.P.; Solari, G. The annual rate of independent events–A key interpretation for traditional extreme value distributions of wind velocity. *Wind Energy* **2022**, *25*, 1188–1202. [CrossRef]
21. Li, J.; Liu, M.; Yan, X.; Yang, Q. Statistical analysis of wind load probabilistic models considering wind direction and calculation of reference wind pressure values in Liaoning Province, China. *Probabilistic Eng. Mech.* **2024**, *75*, 103550. [CrossRef]
22. Masseran, N. Integrated approach for the determination of an accurate wind-speed distribution model. *Energy Convers. Manag.* **2018**, *173*, 56–64. [CrossRef]
23. Wang, Y.; Li, Y.; Zou, R.; Song, D. Bayesian infinite mixture models for wind speed distribution estimation. *Energy Convers. Manag.* **2021**, *236*, 113946. [CrossRef]
24. Aries, N.; Boudia, S.M.; Ounis, H. Deep assessment of wind speed distribution models: A case study of four sites in Algeria. *Energy Convers. Manag.* **2018**, *155*, 78–90. [CrossRef]
25. Jung, C.; Schindler, D. Development of a statistical bivariate wind speed-wind shear model (WSWS) to quantify the height-dependent wind resource. *Energy Convers. Manag.* **2017**, *149*, 303–317. [CrossRef]
26. Han, Q.; Hao, Z.; Hu, T.; Chu, F. Non-parametric models for joint probabilistic distributions of wind speed and direction data. *Renew. Energy* **2018**, *126*, 1032–1042. [CrossRef]
27. Shi, H.; Dong, Z.; Xiao, N.; Huang, Q. Wind speed distributions used in wind energy assessment: A review. *Front. Energy Res.* **2021**, *9*, 769920. [CrossRef]
28. Jung, C.; Schindler, D. Changing wind speed distributions under future global climate. *Energy Convers. Manag.* **2019**, *198*, 111841. [CrossRef]
29. Manis, P.; Bloodworth, A.G. Climate change and extreme wind effects on transmission towers. *Proc. Inst. Civ. Eng.-Struct. Build.* **2017**, *170*, 81–97. [CrossRef]
30. Kim, H.; Kim, S.; Shin, H.; Heo, J.-H. Appropriate model selection methods for nonstationary generalized extreme value models. *J. Hydrol.* **2017**, *547*, 557–574. [CrossRef]
31. Agilan, V.; Umamahesh, N. Modelling nonlinear trend for developing non-stationary rainfall intensity–duration–frequency curve. *Int. J. Climatol.* **2017**, *37*, 1265–1281. [CrossRef]
32. Ragno, E.; AghaKouchak, A.; Cheng, L.; Sadegh, M. A generalized framework for process-informed nonstationary extreme value analysis. *Adv. Water Resour.* **2019**, *130*, 270–282. [CrossRef]
33. Solari, S.; Losada, M.Á. Simulation of non-stationary wind speed and direction time series. *J. Wind Eng. Ind. Aerodyn.* **2016**, *149*, 48–58. [CrossRef]
34. Zeng, M.; Li, J.-H.; Meng, Q.-H.; Zhang, X.-N. Temporal-spatial cross-correlation analysis of non-stationary near-surface wind speed time series. *J. Cent. South Univ.* **2017**, *24*, 692–698. [CrossRef]
35. Wang, L.; Li, J. Estimation of extreme wind speed in SCS and NWP by a non-stationary model. *Theor. Appl. Mech. Lett.* **2016**, *6*, 131–138. [CrossRef]
36. Huang, Z.-F.; Xia, Y.; Gu, M.; Fu, G.-Q. Estimating a joint probability distribution model of fluctuating wind speeds of monsoons from field-measured wind speed data. *J. Wind. Eng. Ind. Aerodyn.* **2022**, *227*, 105054. [CrossRef]
37. Natarajan, N.; Vasudevan, M.; Rehman, S. Evaluation of suitability of wind speed probability distribution models: A case study from Tamil Nadu, India. *Environ. Sci. Pollut. Res.* **2022**, *29*, 85855–85868. [CrossRef] [PubMed]
38. Wang, W.-X.; Chen, K.-X.; Bai, Y.; Chen, Y.; Wang, J.-W. New estimation method of wind power density with three-parameter Weibull distribution: A case on Central Inner Mongolia suburbs. *Wind Energy.* **2022**, *25*, 368–386. [CrossRef]
39. Kikumoto, H.; Ooka, R.; Sugawara, H.; Lim, J. Observational study of power-law approximation of wind profiles within an urban boundary layer for various wind conditions. *J. Wind Eng. Ind. Aerodyn.* **2017**, *164*, 13–21. [CrossRef]
40. Stuart, A.; Ord, K. *Kendall's Advanced Theory of Statistics, Distribution Theory*; John Wiley & Sons: Hoboken, NJ, USA, 2010; Volume 1.
41. Gao, Z.; Fu, Y.; Li, Y.; Liu, J.; Chen, N.; Zhang, X. Trends of streamflow, sediment load and their dynamic relation for the catchments in the middle reaches of the Yellow River over the past five decades. *Hydrol. Earth Syst. Sci.* **2012**, *16*, 3219–3231. [CrossRef]
42. Aslam, M.; Albassam, M. Forecasting of wind speed using an interval-based least square method. *Front. Energy Res.* **2022**, *10*, 896217. [CrossRef]
43. Coles, S.; Bawa, J.; Trenner, L.; Dorazio, P. *An Introduction to Statistical Modeling of Extreme Values*; Springer: Berlin/Heidelberg, Germany, 2001; Volume 208.
44. Rasmussen, M.H.; Duan, C.; Kulik, H.J.; Jensen, J.H. Uncertain of uncertainties? A comparison of uncertainty quantification metrics for chemical data sets. *J. Cheminform.* **2023**, *15*, 121. [CrossRef] [PubMed]
45. Lin, L.-C.; Huang, P.-H.; Weng, L.-J. Selecting path models in SEM: A comparison of model selection criteria. *Struct. Equ. Model. A Multidiscip. J.* **2017**, *24*, 855–869. [CrossRef]
46. Huang, P.-H. Asymptotics of AIC, BIC, and RMSEA for model selection in structural equation modeling. *Psychometrika* **2017**, *82*, 407–426. [CrossRef] [PubMed]

47. Chen, Y.R.; Chu, P.S. Trends in precipitation extremes and return levels in the Hawaiian Islands under a changing climate. *Int. J. Climatol.* **2014**, *34*, 3913–3925. [CrossRef]
48. Katz, R.W.; Parlange, M.B.; Naveau, P. Statistics of extremes in hydrology. *Adv. Water Resour.* **2002**, *25*, 1287–1304. [CrossRef]
49. Gilleland, E.; Katz, R.W. extRemes 2.0: An extreme value analysis package in R. *J. Stat. Softw.* **2016**, *72*, 1–39. [CrossRef]
50. Cheng, L.; AghaKouchak, A.; Gilleland, E.; Katz, R.W. Non-stationary extreme value analysis in a changing climate. *Clim. Chang.* **2014**, *127*, 353–369. [CrossRef]
51. *GB 50009-2012*; Load Code for the Design of Building Structures. China Architecture and Building Press: Beijing, China, 2012.
52. Li, Z.; Song, L.; Ma, H.; Xiao, J.; Wang, K.; Chen, L. Observed surface wind speed declining induced by urbanization in East China. *Clim. Dyn.* **2018**, *50*, 735–749. [CrossRef]
53. Xia, D.; Nie, H.; Sun, L.; Wang, J.; Chow, K.-C.; Chan, K.-L.; Wang, D. Urbanization effects on surface wind in the Guangdong–Hong Kong–Macao Greater Bay area using a fan-sector method. *Int. J. Environ. Res. Public Health* **2022**, *19*, 3194. [CrossRef]
54. Morris, M.; Kushner, P.J.; Moore, G.; Mercan, O. Atmospheric Circulation Patterns Associated with Extreme Wind Events in Canadian Cities. *J. Clim.* **2023**, *36*, 4443–4460. [CrossRef]
55. Gould, B.; Burris, D. Effects of wind shear on wind turbine rotor loads and planetary bearing reliability. *Wind Energy* **2016**, *19*, 1011–1021. [CrossRef]
56. Nadarajah, S. Extremes of daily rainfall in West Central Florida. *Clim. Chang.* **2005**, *69*, 325–342. [CrossRef]
57. Leclerc, M.; Ouarda, T.B. Non-stationary regional flood frequency analysis at ungauged sites. *J. Hydrol.* **2007**, *343*, 254–265. [CrossRef]

Disclaimer/Publisher's Note: The statements, opinions and data contained in all publications are solely those of the individual author(s) and contributor(s) and not of MDPI and/or the editor(s). MDPI and/or the editor(s) disclaim responsibility for any injury to people or property resulting from any ideas, methods, instructions or products referred to in the content.